NASA Technical Memorandum 4770

Thermal and Mechanical Buckling Analysis of Hypersonic Aircraft Hat-Stiffened Panels with Varying Face Sheet Geometry and Fiber Orientation

William L. Ko
Dryden Flight Research Center
Edwards, California

National Aeronautics and
Space Administration
Office of Management
Scientific and Technical
Information Program
1996

NASA Technical Memorandum 4770

Thermal and Mechanical Buckling Analysis of Hypersonic Aircraft Hat-Stiffened Panels with Varying Face Sheet Geometry and Fiber Orientation

William L. Ko

December 1996

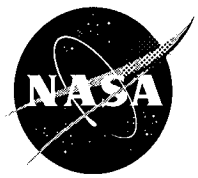

CONTENTS

TABLES

FIGURES

Page

ABSTRACT

Mechanical and thermal buckling behavior of monolithic and metal-matrix composite hat-stiffened panels were investigated. The panels have three types of face-sheet geometry: flat face sheet, microdented face sheet, and microbulged face sheet. The metal-matrix composite panels have three types of face-sheet layups, each of which is combined with various types of hat composite layups. Finite-element method was used in the eigenvalue extractions for both mechanical and thermal buckling. The thermal buckling analysis required both eigenvalue and material property iterations. Graphical methods of the dual iterations are shown. The mechanical and thermal buckling strengths of the hat-stiffened panels with different face-sheet geometry are compared. It was found that by just microdenting or microbulging of the face sheet, the axial, shear, and thermal buckling strengths of both types of hat-stiffened panels could be enhanced considerably. This effect is more conspicuous for the monolithic panels. For the metal-matrix composite panels, the effect of fiber orientations on the panel buckling strengths was investigated in great detail, and various composite layup combinations offering high panel buckling strengths are presented. The axial buckling strength of the metal-matrix panel was sensitive to the change of hat fiber orientation. However, the lateral, shear, and thermal buckling strengths were insensitive to the change of hat fiber orientation.

NOMENCLATURE

A	cross-sectional area of unit strip of hat-stiffened panel, in^2
A_{i-1}, A_i	cross-sectional areas of two adjacent finite elements at node i, in^2
A_h	cross-sectional area of hat finite element at juncture of face sheet and hat, in^2
a	one-half of hat base width, in.
b	one-half of hat top width, in.
d	amount of microdent or microbulge of face sheet, in.
E	Young's modulus of monolithic material, lb/in^2
E_{11}	longitudinal modulus of elasticity of metal-matrix composite lamina, lb/in^2
E_{22}	transverse modulus of elasticity of metal-matrix composite lamina, lb/in^2
E43	quadrilateral combined membrane and bending element
F_x	axial compressive load, lb
G	shear modulus of monolithic material, lb/in^2
G_{12}	shear modulus of metal-matrix composite lamina, lb/in^2
h	depth of hat-stiffened panel, in.
JLOC	joint location (node or grid point)
L_{i-1}, L_i	widths of two adjacent finite elements at node i, in.
MMC	metal-matrix composite
N_x	effective panel load in hat axial direction, lb/in.

N_{xy}	panel shear load, lb/in.
N_y	panel load transverse to hat axial direction, lb/in.
n	integer
P_i	axial compressive nodal force at node i, lb
p	half-width of unit hat strip, in.
Q_i	lateral compressive nodal force at node i, lb
R_i	shear nodal force at node i, lb
r	radius of circular arc regions of hat corrugation leg, in.
SPAR	structural performance and resizing finite-element computer program
T	temperature, °F
T_a	assumed temperature for materials, °F
T_r	room temperature (70 °F)
t_c	thickness of reinforcing hat, in.
t_s	thickness of face sheet, in.
x, y, z	rectangular Cartesian coordinates
ZERO	SPAR program constraint command
α	coefficient of thermal expansion of monolithic material, in/in-°F
α_{11}	longitudinal coefficient of thermal expansion of metal-matrix composite lamina, in/in-°F
α_{12}	coefficient of thermal shear distortion of metal-matrix composite lamina, in/in-°F
α_{22}	transverse coefficient of thermal expansion of metal-matrix composite lamina, in/in-°F
ΔT	temperature increase, °F
θ	fiber orientation angle measured from x-axis, degree
λ_j	eigenvalue at jth iteration
λ_x	eigenvalue for axial buckling
λ_y	eigenvalue for lateral buckling
λ_{xy}	eigenvalue for shear buckling
λ_T	eigenvalue for thermal buckling
ν	Poisson ratio of monolithic material
ν_{12}	Poisson ratio of metal-matrix composite lamina
σ_x	axial compressive stress distributed over the entire cross-sectional area of the unit strip of hat-stiffened panel, lb/in^2

Subscripts

cr	critical value at buckling
flat	value associated with flat face sheet case
n	*n*th iteration for updating input material properties

INTRODUCTION

Structural panels for hypersonic flight vehicles are subjected to both aerodynamic load (mechanical load) and aerodynamic heating (thermal load). The thermal load can be quite critical at hypersonic velocities. Therefore, the hot-structural panels must be designed to maximize the stiffness and, at the same time, to minimize the thermal expansion-induced problems. Several hot-structural panel concepts considered and evaluated both theoretically and experimentally in the past include: (1) beaded panels (ref. 1), (2) tubular panels (refs. 2 and 3) high-temperature alloy honeycomb-core sandwich panels (refs. 3 through 6), and (4) hat-stiffened panels (refs. 7 through 13).

Recently, the hat-stiffened panels, fabricated with either monolithic titanium alloy or metal-matrix composites (MMCs) were analyzed and tested extensively to understand their buckling characteristics under different thermal environments (refs. 7 through 13). The face sheet of the test panels were either flat or microbeaded (or microdented). The hat-stiffened panels with microbeaded face sheets offer considerably higher buckling strength compared with the flat face sheet panels. However, further study on the effect of various structural design parameters will help define an optimum structural configuration for the hat-stiffened panel concept.

This report deals with the finite-element thermal and mechanical buckling analysis of a unit strip of hat-stiffened panels fabricated with either monolithic titanium alloy or with MMC. The face-sheet geometry analyzed is similar in construction to those considered in the past, with either flat or microdented face sheets. Additionally, hat-stiffened panels with microbulged face sheets are explored. This report presents the results of an investigation into the effects of both microdenting and microbulging of the face sheet on the buckling strengths of the hat-stiffened panels. For MMC hat-stiffened panels with flat face sheets, the effects of composite fiber orientation on the panel buckling strengths are studied, and various composite layup combinations offering high panel buckling strengths are discussed.

DESCRIPTION OF PROBLEM

Figure 1 shows one of the hat-stiffened panels. The panel face sheet has three types of geometry: flat face sheet, microdented face sheet, and microbulged face sheet. The panels are fabricated with either monolithic or MMC material. Figure 2 shows the cross-sectional shapes of the unit strips of the three types of the hat-stiffened panels. The unit strip has width $2p$, depth h, and the face sheet and hat have thicknesses t_s and t_c, respectively. The cross-section of the microdent or microbulge of the face sheet is circular arc in shape with d indicating the degree of microdent or microbulge.

For the MMC panels, three cases of face sheet layups are considered, each of which is combined with various hat layups (fig. 3). Table 1 lists the MMC layup combinations studied.

Table 1. MMC layup combinations.

Face-sheet layup	Hat layup
[90/0/0/90]	[θ/–θ/–θ/θ] [90/0/0/90] [0/90/90/0]
[0/90/90/0]	
[45/–45/–45/45]	

In table 1, θ is the fiber orientation angle measured from the x-axis (fig. 3), ranging from 0 to 90 degrees.

The present study uses the finite-element method to analyze the unit strip of hat-stiffened panel:

1. To investigate the effect of microdent and microbulge on the thermal and mechanical buckling strengths of the monolithic and the MMC hat-stiffened panels.
2. To investigate the effect of composite layups on the thermal and mechanical buckling strengths of the MMC hat-stiffened panels.
3. To identify the type of MMC layup combination that would give the optimum panel buckling strength for design of hypersonic vehicles.

FINITE-ELEMENT MODELING

The structural performance and resizing (SPAR) computer program (ref. 14) was used in the finite-element analysis. For each type of hat-stiffened panel, only one unit strip of the panel was considered (fig. 4). For axial, lateral, and thermal buckling, one-quarter of the unit strip was modeled, and symmetry commands were used to generate the whole strip. If the lowest buckling mode was antisymmetrical, then the antisymmetry command in the SPAR program was used instead of the symmetry command. For shear buckling, the whole unit strip was modeled because the symmetry and antisymmetry commands could not be used. Figure 5 shows a typical quarter-strip, finite-element model adjusted for the microbulged face sheet panel. The model has 1596 joint locations (JLOCs) and 1500 E43 elements (quadrilateral combined membrane and bending elements). Figure 6 shows a typical whole-strip, finite-element model adjusted for the microbulged-face sheet panel for shear-buckling analysis. The model has 3040 JLOCs and 3000 E43 elements.

BOUNDARY CONDITIONS

For all four loading conditions (described as follows), the rotation with respect to the z-axis at every node of each model was constrained using the SPAR constraint command ZERO 6, where 6 denotes the conventional 6th degree of freedom. When the commands SYMMETRY PLANE = 1 (yz-plane) and SYMMETRY PLANE = 2 (xz-plane) were used for the quarter-strip model to generate the mirror images, the SPAR program automatically imposes internally the constraints ZERO 1, 5 and ZERO 2, 4, respectively, for the yz- and xz-planes of symmetry.

Axial Buckling

Axial buckling is buckling in the hat axial direction (i.e., x-direction). Figure 7 shows all the constraint conditions for the quarter-strip panel for axial buckling. Because the unit hat strip is part of the whole panel, the closest boundary constraints were chosen to approximate the actual condition of the unit hat strip, which is surrounded by the rest of the whole panel. Thus, at the ends of the unit strip, constraint ZERO 3, 5 was imposed at the face sheet and hat flat regions. Along the long edges of the face sheet, constraint ZERO 2, 4 was imposed to allow the unit strip to deform freely in the z-direction, like the whole panel.

Lateral Buckling

Lateral buckling is buckling in the direction transverse to the hat axial direction (i.e., y-direction). Figure 8 shows the constraint commands for lateral buckling. The two long edges of the face sheet are simply supported (i.e., constraint ZERO 3). This edge condition could give the buckling mode shape similar to the whole-panel case. At each end of the face sheet and hat flat regions, constraint ZERO 1, 3, 5 was imposed.

Shear Buckling

Figure 9 shows the constraint conditions for shear buckling of the whole unit strip. One long edge is fixed with constraint ZERO 1, 2, 3, 4; the other with constraint ZERO 2, 3, 4. The ends of the face sheet are constrained with ZERO 3, 5. The ends of the hat are unconstrained.

Thermal Buckling

Figure 10 shows the constraint conditions for thermal buckling. The long side of the face sheet is constrained with ZERO 2, 3, 4; the ends of the face sheet and hat flat region with constraint ZERO 1, 3, 5.

APPLIED LOADS

Axial Buckling

For axial buckling, an unit axial compressive load F_x = 1 lb was applied. This axial load was distributed over the nodes of the cross-section of the unit strip (i.e., face sheet and hat cross-sections; fig. 11) to generate an uniform axial compressive stress of

$$\sigma_x = \frac{F_x}{A} = \frac{1}{A} \tag{1}$$

where A is the cross-sectional area of the unit strip. The effective panel load N_x for the unit strip is defined as

$$N_x = \frac{F_x}{2p} = \frac{1}{2p} \tag{2}$$

The input nodal force P_i at node i of a finite-element model is calculated from

$$P_i = \frac{1}{2}(A_{i-1} + A_i)\sigma_x \tag{3}$$

where A_{i-1} and A_i are the cross-sectional areas of the two adjacent elements at node i.

If the node i is at the juncture where the face sheet and hat meet, the nodal force P_i is calculated from

$$P_i = \frac{1}{2}(A_{i-1} + A_i + A_h)\sigma_x \tag{4}$$

where A_h is the cross-sectional area of the hat element adjacent to the juncture node i.

If the node i is at the corner of the face sheet, then P_i is calculated from

$$P_i = \frac{1}{2}A_i\sigma_x \tag{5}$$

Lateral Buckling

For lateral buckling, the panel lateral compressive load N_y = 1 lb/in. was applied only to the long edges of the face sheet. The lateral compressive nodal force Q_i at node i is then calculated from

$$Q_i = \frac{1}{2}(L_{i-1} + L_i)N_y \tag{6}$$

where L_{i-1} and L_i are the widths of the two adjacent edge elements at node i.

When node i is at the corner of the face sheet, equation (6) becomes

$$Q_i = \frac{1}{2}L_iN_y \tag{7}$$

Shear Buckling

For shear buckling, the panel shear load N_{xy} = 1 lb/in. was applied at the edges of the face sheet only. The shear nodal force R_i at node i was calculated from

$$R_i = \frac{1}{2}(L_{i-1} + L_i)N_{xy} \tag{8}$$

or

$$R_i = \frac{1}{2}L_iN_{xy} \tag{9}$$

if node i is at the corner of the face sheet.

Thermal Buckling

For thermal buckling, the panel was subjected to a uniform temperature field. The uniform nodal temperature of ΔT = 1 °F was used as thermal load input to every node of the finite-element models.

In calculating buckling temperature ΔT_{cr}, a problem is that the input material properties, which are temperature dependent, must correspond to the unknown buckling temperature $\Delta T_{cr} + T_r$, where T_r is room temperature (70 °F). For this reason, one has to assume a temperature T_a, and use the material properties corresponding to T_a as inputs to calculate ΔT_{cr}. This material property iteration process must continue until the assumed temperature T_a approaches the calculated buckling temperature $\Delta T_{cr} + T_r$. Thus, the thermal buckling solution process requires both eigenvalue and material property iterations.

BUCKLING LOADS AND TEMPERATURES

If λ_x, λ_y, λ_{xy}, and λ_T are the lowest eigenvalues for the axial, lateral, shear, and thermal buckling cases, respectively, then the buckling loads $(N_x)_{cr}$, $(N_y)_{cr}$, $(N_{xy})_{cr}$, and the buckling temperature ΔT_{cr} associated with the four buckling cases may be obtained by multiplying the respective applied loads and temperature by the corresponding eigenvalues (i.e., scaling factors) as

$$(N_x)_{cr} = \lambda_x N_x = \frac{\lambda_x}{2p} ; \qquad N_x = \frac{1}{2p} \tag{10}$$

$$(N_y)_{cr} = \lambda_y N_y = \lambda_y ; \qquad N_y = 1 \tag{11}$$

$$(N_{xy})_{cr} = \lambda_{xy} N_{xy} = \lambda_{xy} ; \qquad N_{xy} = 1 \tag{12}$$

$$\Delta T_{cr} = \lambda_T \Delta T = \lambda_T ; \qquad \Delta T = 1 \tag{13}$$

In the eigenvalue extractions that the SPAR program uses, the iterative process consists of a Stodola matrix iteration procedure, followed by a Rayleigh-Ritz procedure, and finally a second Stodola procedure. This process results in successively refined approximations of m eigenvectors associated with the m eigenvalues. Reference 14 describes the detail of this process.

NUMERICAL EXAMPLES

Tables 2 and 3 show geometrical dimensions and material properties, respectively, for the monolithic and the metal-matrix composite hat-stiffened panels.

Table 2. Geometry of the hat-stiffened panel.

a	=	0.64 in.
b	=	0.4 in.
d	=	0.015 or 0.03 in.
h	=	1.25 in.
p	=	1.46 in.
r	=	0.33 in.
t_c	=	0.032 in.
t_s	=	0.032 in.

Note that two values of d were used for the microdented and microbulged face-sheet cases.

Table 3. Temperature-dependent material properties for monolithic titanium (Ti-6Al-4V, ref. 15).

	70 °F	200 °F	300 °F	400 °F	500 °F	600 °F	700 °F	800 °F	900 °F	1000 °F
E, lb/in$^2 \times 10^6$	16.0	15.28	14.80	14.40	14.02	13.63	13.15	12.64	11.84	10.56
G, lb/in$^2 \times 10^6$	6.20	5.83	5.65	5.50	5.37	5.20	5.02	4.82	4.52	4.03
ν	0.31	0.31	0.31	0.31	0.31	0.31	0.31	0.31	0.31	0.31
α, in/in-°F $\times 10^{-6}$	4.85	5.00	5.10	5.19	5.27	5.36	5.44	5.52	5.59	5.62

The data in table 4 were plotted in figure 12 to show the nonlinearity of the temperature-dependent material property curves.

Table 4. Temperature-dependent material properties for metal-matrix composite.

	70 °F	1200 °F
E_{11}, lb/in^2	27.72×10^6	23.22×10^6
E_{22}, lb/in^2	18.08×10^6	8.69×10^6
G_{12}, lb/in^2	8.15×10^6	3.5×10^6
ν_{12}	0.3	0.3
α_{11}, in/in-°F	2.16×10^{-6}	3.21×10^{-6}
α_{22}, in/in-°F	4.61×10^{-6}	6.15×10^{-6}
α_{12}, in/in-°F	0.0	0.0

MATERIAL PROPERTY ITERATIONS

Monolithic Panels

As mentioned earlier, calculations of buckling temperatures require material property iterations. Figure 13 illustrates the iteration process for calculation of buckling temperatures ΔT_{cr} for a panel with a microdented face sheet. The calculated buckling temperature ΔT_{cr} is plotted against the assumed temperature T_a for the material properties. The 45-degree line represents the solution line for the buckling temperature ΔT_{cr}. For example, if the assumed material temperature T_a agrees with the calculated buckling temperature $\Delta T_{cr} + T_r$, then the data point of ΔT_{cr} falls right on the 45-degree line. In the first iteration, the material properties at, for example, $(T_a)_1 = T_r = 70$ °F was used to calculate the first buckling temperature $(\Delta T_a)_1$. The second iteration then uses the material properties at any other temperature, for example, $(T_a)_2 = 300$ °F, to update the input material properties to calculate the second buckling temperature $(\Delta T_{cr})_2$. In the third iteration, the two data points $(\Delta T_{cr})_1$ and $(\Delta T_{cr})_2$ were connected

with a straight line to locate the intersection point with the 45-degree line, and then this intersection-point temperature was used to update the material properties for calculation of the third buckling temperature $(\Delta T_{cr})_3$. This iteration process continues until the nth-calculated buckling temperature $(\Delta T_{cr})_n$ data point falls right on the 45-degree solution line.

From the geometry of figure 9, $(\Delta T_{cr})_3$ may be expressed as a function of $(\Delta T_{cr})_1$ and $(\Delta T_{cr})_2$ as

$$(\Delta T_{cr})_3 = \frac{(\Delta T_{cr})_1}{1 - \dfrac{(\Delta T_{cr})_2 - (\Delta T_{cr})_1}{(T_a)_2 - (T_a)_1}} \tag{14}$$

For the present monolithic material, the $(\Delta T_{cr})_3$ data point (less than 400 °F) falls practically on the 45-degree solution line, giving an acceptable solution for ΔT_{cr} (less than 0.5 percent error). That is, the value of $(\Delta T_{cr})_3$ calculated from the third material iteration practically agrees with that obtained from equation (14), because the material property curves (fig. 12) are almost linear in the range $0 < T < 500$ °F.

Metal-Matrix Composite Panels

Because of the lack of material data between room temperature and 1200 °F, linear interpolation was used to find the material properties at any temperature. Figure 14 shows the material property iteration process for a typical composite panel with [90/0/0/90] flat face sheet and [45/–45/–45/45] hat. Similar to the monolithic case, in the first iteration, the $(\Delta T_{cr})_1$ data point was calculated using the room-temperature material properties. In calculating $(\Delta T_{cr})_2$, a new temperature $(T_a)_2 = (\Delta T_{cr})_1 + (T_a)_1$ {where $(T_a)_1 = T_r$}, instead of any temperature on the right-hand side of the 45-degree line, was used to update the input material properties. Because the coefficients of thermal expansion α_{ij} increase with temperature, $(\Delta T_{cr})_2$ would fall below the 45-degree line. In the third iteration, similar to the monolithic case, the two data points $(\Delta T_{cr})_1$ and $(\Delta T_{cr})_2$ were connected with a straight line that intersects the 45-degree solution line. Then, the temperature at the intersection point was used to update the material properties for the calculations of the third data point $(\Delta T_{cr})_3$. Because of the linear interpolation of the material properties, the $(\Delta T_{cr})_3$ data point falls right on the 45-degree solution line, giving the desired thermal buckling solution.

The value of $(\Delta T_{cr})_3$ obtained from the material iteration process may be compared with the value of $(\Delta T_{cr})_3$ calculated from

$$(\Delta T_{cr})_3 = \frac{(\Delta T_{cr})_1}{2 - \dfrac{(\Delta T_{cr})_2}{(\Delta T_{cr})_1}} \tag{15}$$

which was established using figure 14.

RESULTS

In the finite-element buckling analysis, the eigenvalue iterations were terminated if the convergence control criterion $[(\lambda_j - \lambda_{j-1})/\lambda_j] < 10^{-5}$ was reached. The following subsections present numerical results of the buckling analysis for the different types of hat-stiffened panels.

Monolithic Panels

Figures 15 through 18, respectively, show the buckled shapes of the three types of monolithic hat-stiffened panels under axial compressive, lateral compressive, shear, and thermal loadings. For axial buckling (fig. 15) and thermal buckling (fig. 18), microbulging of the face sheet increased the number of buckles more than microdenting of the face sheet. For lateral and shear buckling (figs. 16 and 17), the buckle number is not affected by microdenting or microbulging.

Table 5 summarizes the mechanical buckling loads and thermal buckling temperatures calculated for different types of monolithic hat-stiffened panels.

Table 5. Buckling loads and buckling temperatures of monolithic hat-stiffened panels.

Buckling load or buckling temperature	Face-sheet type				
	Flat	Microdented		Microbulged	
		d	$2d$	d	$2d$
$(N_x)_{cr}$, lb/in.	1979.69	2451.33	3563.42	2471.87	3583.46
$(N_x)_{cr}/(N_x)_{cr}\|_{flat}$	1.0	1.2382	1.7999	1.2486	1.8101
$(N_y)_{cr}$, lb/in.	270.04	269.76	270.50	272.03	275.00
$(N_y)_{cr}/(N_y)_{cr}\|_{flat}$	1.0	0.9990	1.0017	1.0074	1.0184
$(N_{xy})_{cr}$, lb/in.	912.43	1208.60	2023.15	1218.87	2073.01
$(N_{xy})_{cr}/(N_{xy})_{cr}\|_{flat}$	1.0	1.3246	2.2173	1.3359	2.2720
ΔT_{cr}, °F	116.56	188.15	350.48	188.17	352.75
$\Delta T_{cr}/\Delta T_{cr}\|_{flat}$	1.0	1.6142	3.0069	1.6144	3.0263

The data given in table 4 are plotted in figures 19 and 20 for better visualization of the effect of microdenting or microbulging on the panel buckling strengths. Notice that by microdenting or microbulging the face sheet by an amount slightly less than the face-sheet thickness, the axial and shear buckling loads $\{(N_x)_{cr}, (N_{xy})_{cr}\}$ and the buckling temperature ΔT_{cr} could be increased considerably. However,

the lateral buckling load $(N_y)_{cr}$ is practically unaffected by microdenting or microbulging of the face sheet. The microbulged face-sheet case appears to be slightly more buckling efficient than the microdented face-sheet case, which may be attributed to the increase in the moment of inertia about the neutral axis. In actual applications, either the axis of the face-sheet microdent (or microbulge) is parallel to the free stream (fuselage-panel case) or normal to the freestream direction (wing-panel case), and the degree of aerodynamic heating disturbance that the microdenting (or microbulging) causes remains to be investigated.

Metal-Matrix Composite Panels

The buckled shapes of the MMC hat-stiffened panels are very similar to those of the monolithic cases and, therefore, are not shown. Table 6 summarizes the mechanical and thermal buckling data for the composite panels with different degrees of face-sheet microdent or microbulge. The composite panels chosen for this study have [90/0/0/90] face-sheet and [45/–45/–45/45] hat layups.

Table 6. Buckling loads and buckling temperatures of MMC hat-stiffened panels with [90/0/0/90] face sheet and [45/–45/–45/45] hat.

Buckling load or buckling temperature	Face-sheet type				
	Flat	Microdented		Microbulged	
		d	$2d$	d	$2d$
$(N_x)_{cr}$, lb/in.	2944.39	3344.24	4337.56	3366.47	4399.88
$(N_x)_{cr}/(N_x)_{cr}\|_{flat}$	1.0	1.1358	1.4732	1.1434	1.4943
$(N_y)_{cr}$, lb/in.	715.63	738.31	750.73	724.42	726.12
$(N_y)_{cr}/(N_y)_{cr}\|_{flat}$	1.0	1.0317	1.0490	1.0123	1.0147
$(N_{xy})_{cr}$, lb/in.	1401.33	1709.09	2702.55	1899.04	3075.62
$(N_{xy})_{cr}/(N_{xy})_{cr}\|_{flat}$	1.0	1.2196	1.9286	1.3552	2.1948
ΔT_{cr}, °F	195.18	252.37	413.53	275.96	439.43
$\Delta T_{cr}/\Delta T_{cr}\|_{flat}$	1.0	1.2930	2.1187	1.4139	2.2514

The mechanical and thermal buckling data of table 6 are plotted, respectively, in figures 21 and 22 as functions of the degree of microdent or microbulge d. It is seen that for the composite cases, the benefit of the microdenting or microbulging of the face sheets in increasing the axial and shear buckling loads $\{(N_x)_{cr}, (N_{xy})_{cr}\}$, and the buckling temperatures ΔT_{cr}, is similar to the case for monolithic panels. However, the degree of buckling load improvement is slightly lower for the composite panels (cf., tables 5 and 6). Again, the microbulging of the face sheet is slightly more effective in improving the

panel axial, shear, and thermal buckling strengths than microdenting of the face sheet. Like the monolithic case, the lateral buckling load $(N_y)_{cr}$ is practically unaffected by either microdenting or microbulging of the face sheet.

Table 7 summarizes the mechanical and thermal buckling solutions for the flat-face-sheet, metal-matrix composite, hat-stiffened panels with different layups.

Table 7. Buckling loads and buckling temperatures of MMC hat-stiffened panels with flat face sheets.

Face-sheet layup	Hat layups	$(N_x)_{cr}$, lb/in.	$(N_y)_{cr}$, lb/in.	$(N_{xy})_{cr}$, lb/in.	ΔT_{cr}, °F
90/0/0/90	0/0/0/0	3387.65	722.83	1406.97	189.95
	15/–15/–15/15	3316.96	723.16	1406.41	190.42
	30/–30/–30/30	3140.69	723.66	1404.43	192.45
	45/–45/–45/45	2944.39	715.63	1401.33	194.97
	60/–60/–60/60	2806.54	703.86	1398.01	197.34
	75/–75/–75/75	2740.19	696.19	1395.22	198.75
	90/–90/–90/90	2721.67	693.88	1394.02	200.00
	90/0/0/90	3095.51	728.89	1402.88	195.26
	0/90/90/0	3061.76	718.91	1400.85	194.47
0/90/90/0	0/0/0/0	3462.72	557.09	1072.94	149.71
	15/–15/–15/15	3389.76	557.39	1072.64	150.50
	30/–30/–30/30	3200.16	558.34	1071.39	152.78
	45/–45/–45/45	2991.69	559.90	1069.18	155.70
	60/–60/–60/60	2850.15	561.74	1066.61	158.86
	75/–75/–75/75	2782.44	563.25	1064.27	161.48
	90/–90/–90/90	2764.38	563.83	1063.25	162.57
	90/0/0/90	3149.51	566.31	1069.73	155.92
	0/90/90/0	3114.00	557.41	1068.56	156.23
45/–45/–45/45	0/0/0/0	3662.30	619.45	1256.47	168.36
	15/–15/–15/15	3594.30	619.86	1255.68	169.21
	30/–30/–30/30	3386.48	621.19	1253.19	171.59
	45/–45/–45/45	3169.40	623.37	1249.61	175.11
	60/–60/–60/60	3017.60	625.99	1246.06	177.82
	75/–75/–75/75	2945.04	628.14	1243.24	179.78
	90/–90/–90/90	2938.29	628.97	1242.07	181.06
	90/0/0/90	3341.18	632.31	1251.30	175.04
	0/90/90/0	3300.32	619.66	1249.77	175.14

Figure 23 shows the axial, lateral, and shear buckling loads $\{(N_x)_{cr}, (N_y)_{cr}, (N_{xy})_{cr}\}$, respectively, plotted against the hat-fiber orientation angle θ for the metal-matrix composite, hat-stiffened panels with flat face sheets having three types of layups. In the figure, two types of hat layups, [90/0/0/90] and [0/90/90/0] (indicated by 90/0 and 0/90 on the θ axis, respectively), are added for comparison.

The axial buckling load $(N_x)_{cr}$ decreases with the increase of θ; however, both the lateral and shear buckling loads $\{(N_x)_{cr}, (N_{xy})_{cr}\}$ are insensitive to the change of θ. Notice that for any hat fiber orientation θ, the panels with [45/–45/–45/45] face sheet have the highest axial buckling strength compared with the panels having [90/0/0/90] and [0/90/90/0] face sheets. This phenomenon was also observed in the case of buckling of composite sandwich panels studied by Ko and Jackson earlier (ref. 4).

The buckling strength of the panel depends not only on the longitudinal stiffness but also on the lateral and shear stiffnesses (ref. 5). For this reason, the [45/–45/–45/45] face sheet turned out to provide higher axial buckling strength than the other two types of face sheets. For both lateral and shear buckling, panels with [90/0/0/90] face sheet combined with any hat layup (i.e., θ) ranks at the top among the three face-sheet cases studied.

Based on figure 23, the panel with optimum axial-buckling strength is the one with [45/–45/–45/45] face sheet and [0/0/0/0] hat. However, the [0/0/0/0] unidirectional composite lacks sufficient transverse tensile strength. For practical purposes, the hat layups in the range of 10 deg < θ < 30 deg and the [90/0/0/90] and [0/90/90/0] hats could provide quasi-optimum axial-buckling strength for the panels.

Figure 24 shows the buckling temperature ΔT_{cr} plotted against the hat fiber orientation angle θ for the metal-matrix composite, hat-stiffened panels with flat face sheets having three types of layups. The panels with [90/0/0/90] face sheet give the highest thermal buckling strength among the three face-sheet cases. As shown in the figure, ΔT_{cr} increases slightly with the increase of θ for any face-sheet layup (except for 90/0 and 0/90 hat layup cases).

CONCLUDING REMARKS

Thermal and mechanical buckling characteristics of monolithic and metal-matrix composite hat-stiffened panels were investigated. The study focused on the effect of face-sheet microdenting and microbulging on the panel buckling strengths. Also, for the metal-matrix composite panels, the effect of fiber orientation on the panel buckling strengths was investigated. The key findings of the study are as follows:

1. Microdenting and microbulging of the face sheet could greatly enhance the axial, shear, and thermal buckling strengths of the hat-stiffened panels. However, the lateral buckling strength is not affected by either microdenting or microbulging of the face sheet.
2. Microbulging of the face sheet is slightly more efficient than microdenting of the face sheet in increasing the panel axial, shear, and thermal buckling strengths.
3. For any hat layup, the composite hat-stiffened panels using [45/–45/–45/45] face sheet have higher axial-buckling strengths than those using [90/0/0/90] or [0/90/90/0] face sheet.

4. For the composite panels with any face-sheet layup, the axial buckling strength decreases with the increase of the hat fiber orientation angle. However, the lateral, shear, and thermal buckling loads are insensitive to the change of hat fiber orientation. The composite hat-stiffened panels with [45/–45/–45/45] face sheet combined with [90/0/0/90] hat, [0/90/90/0] hat, or [θ/–θ/–θ/θ] hat (10 deg < θ < 30 deg), offer optimum axial-buckling strength.

5. The effect of microdenting or microbulging on the improvement of buckling strengths is more conspicuous for the monolithic hat-stiffened panels than for the MMC hat-stiffened panels.

Dryden Flight Research Center
National Aeronautics and Space Administration
Edwards, California, April 22, 1996

REFERENCES

1. Siegel, William H., *Experimental and Finite Element Investigation of the Buckling Characteristics of a Beaded Skin Panel for a Hypersonic Aircraft*, NASA CR-144863, April 1978.

2. Ko, William L., John L. Shideler, and Roger A. Fields, *Buckling Characteristics of Hypersonic Aircraft Wing Tubular Panels*, NASA TM-87756, December 1986.

3. Ko, William L. and Raymond H. Jackson, *Thermal Behavior of a Titanium Honeycomb-Core Sandwich Panel*, NASA TM-101732, January 1991.

4. Ko, William L. and Raymond H. Jackson, *Compressive and Shear Buckling Analysis of Metal Matrix Composite Sandwich Panels Under Different Thermal Environments*, NASA TM-4492, June 1993.

5. Ko, William L., *Mechanical and Thermal Buckling Analysis of Rectangular Sandwich Panels Under Different Edge Conditions*, NASA TM-4585, April 1994.

6. Ko, William L., *Predictions of Thermal Buckling Strengths of Hypersonic Aircraft Sandwich Panels Using Minimum Potential Energy and Finite Element Methods*, NASA TM-4643, May 1995.

7. Percy, Wendy C. and Roger A. Fields, "Buckling of Hot Structures," Eighth National Aero-Space Plane Symposium, Naval Postgraduate School, Monterey, California, Mar. 26–30, 1990.

8. Percy, W. and R. Fields, "Buckling Analysis and Test Correlation of Hat Stiffened Panels for Hypersonic Vehicles," AIAA-90-5219, presented at AIAA 2nd International Aerospace Planes Conference, Orlando, Florida, Oct. 29–31, 1990.

9. Teare, Wendy P. and Roger A. Fields, "Buckling Analysis and Test Correlation of High Temperature Structural Panels," *Thermal Structures and Materials for High-Speed Flight*, Earl A. Thornton, ed., vol. 140, Progress in Astronautics and Aeronautics, AIAA, Washington, DC, 1992, pp. 337–352.

10. Ko, William L. and Raymond H. Jackson, *Compressive Buckling Analysis of Hat-Stiffened Panel*, NASA TM-4310, August 1991.

11. Hudson, Larry D. and Randolph C. Thompson, *Single-Strain-Gage Force/Stiffness Buckling Prediction Techniques on a Hat-Stiffened Panel*, NASA TM-101733, February 1991.

12. Thompson, Randolph C. and W. Lance Richards, *Thermal–Structural Panel Buckling Tests*, NASA TM-104243, December 1991.

13. Ko, William L. and Raymond H. Jackson, *Shear Buckling Analysis of a Hat-Stiffened Panel*, NASA TM-4644, November 1994.

14. Whetstone, W.D., *SPAR Structural Analysis System Reference Manual, System Level 13A*, vol. 1, Program Execution, NASA CR-158970-1, December 1978.

15. MIL-Handbook-5B, Aug. 31, 1973.

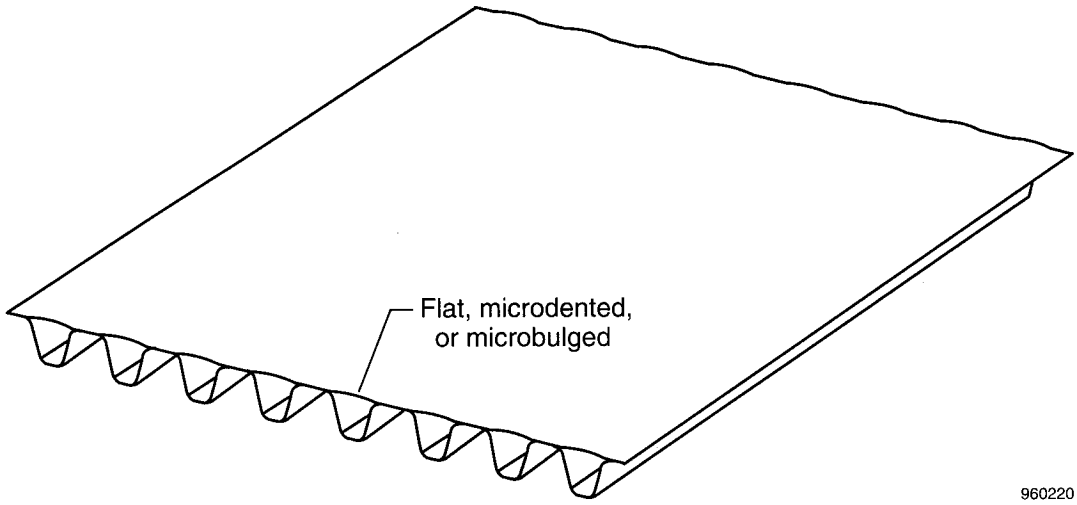

Figure 1. Hat-stiffened panel with flat, microdented, or microbulged face sheet.

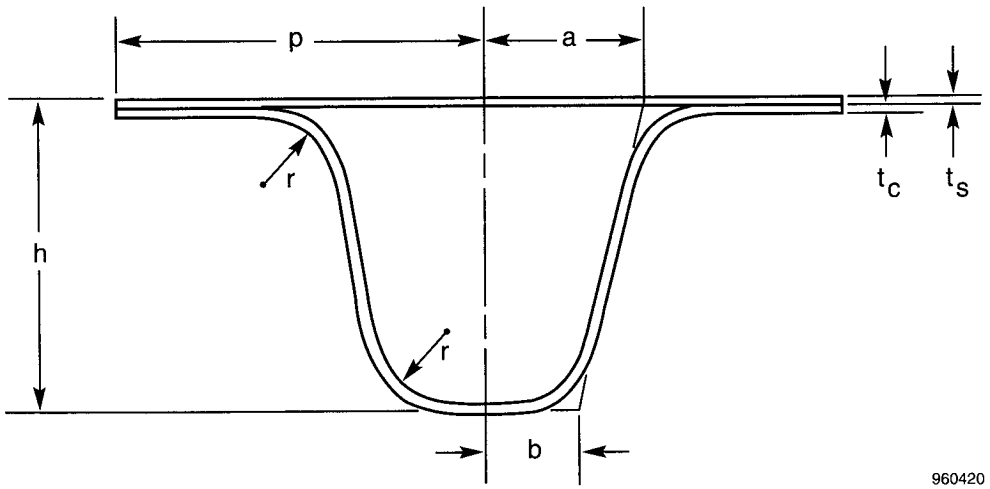

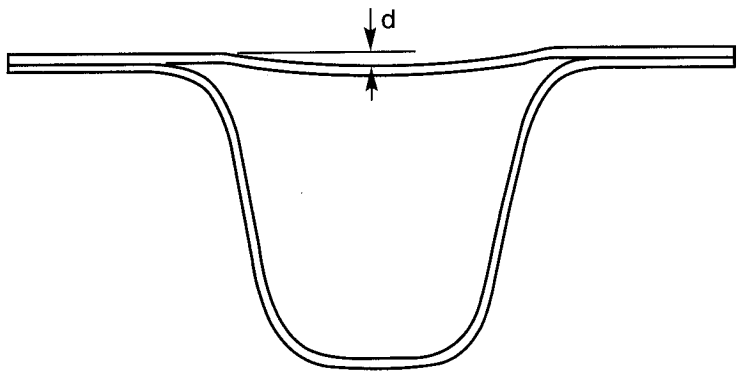

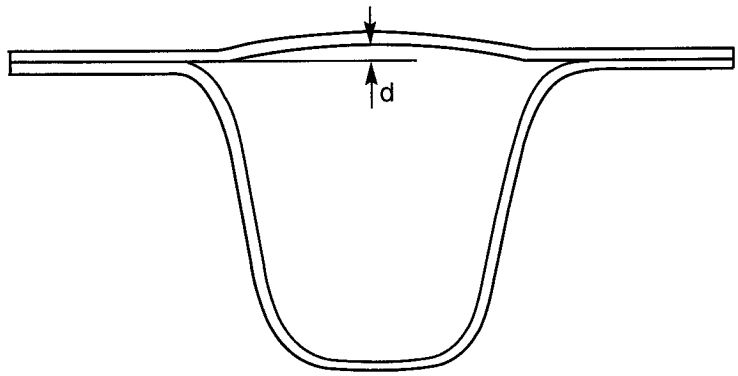

Figure 2. Three types of hat-stiffened panels.

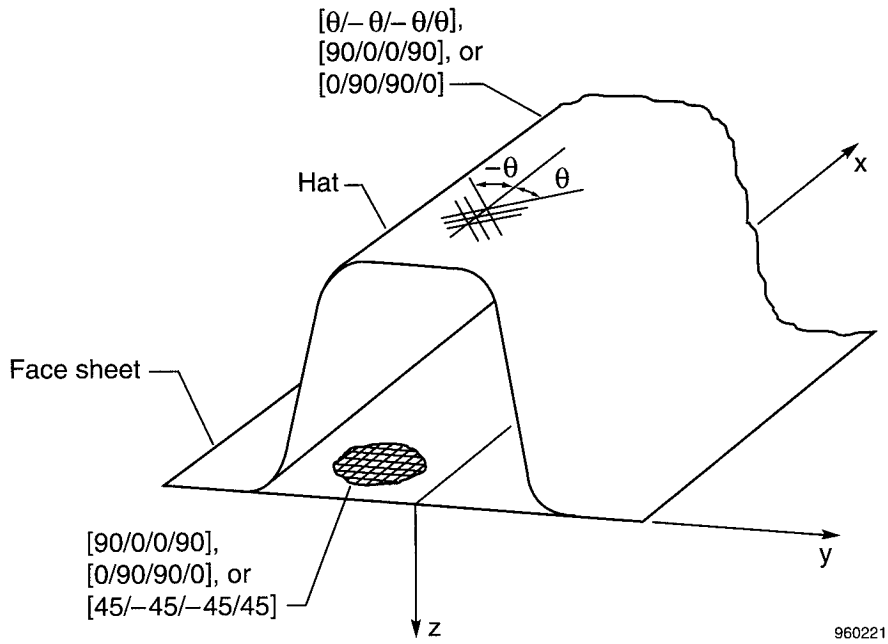

Figure 3. Composite layups for hat-stiffened panels.

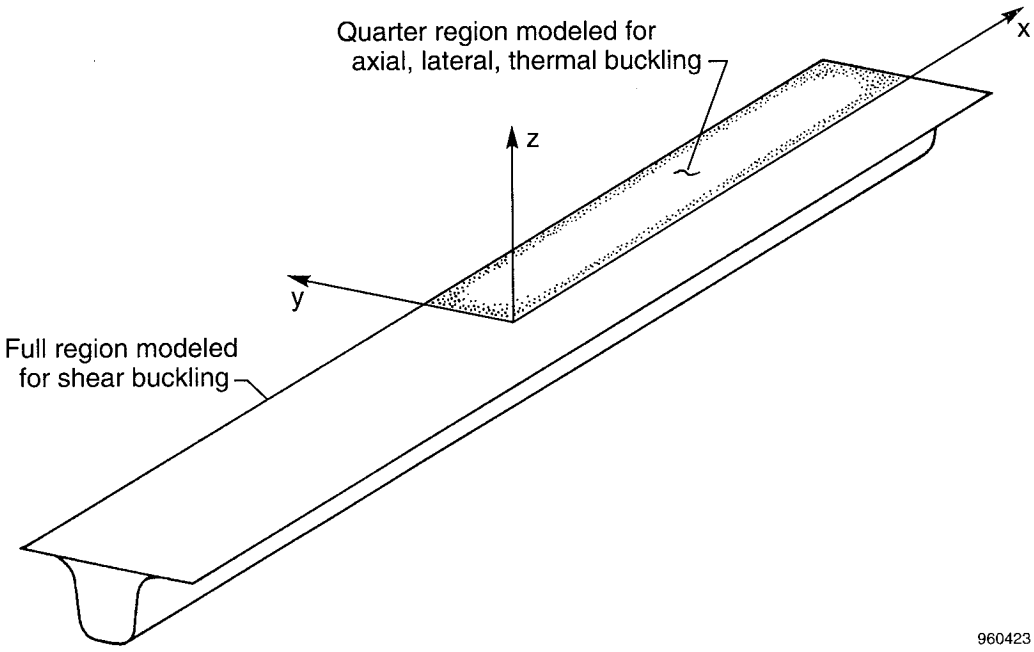

Figure 4. Unit strip of a hat-stiffened panel.

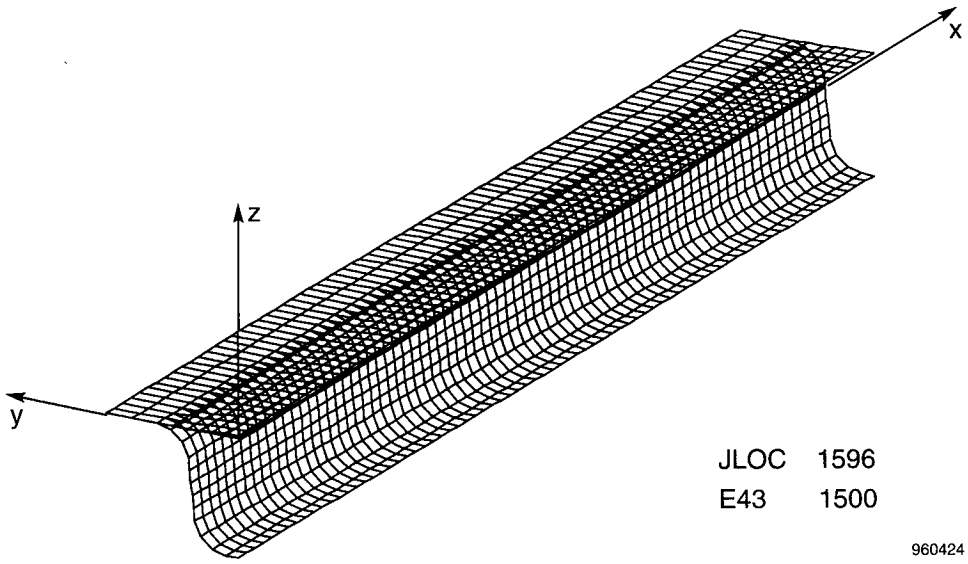

Figure 5. Quarter-unit strip finite-element model; microbulged face sheet.

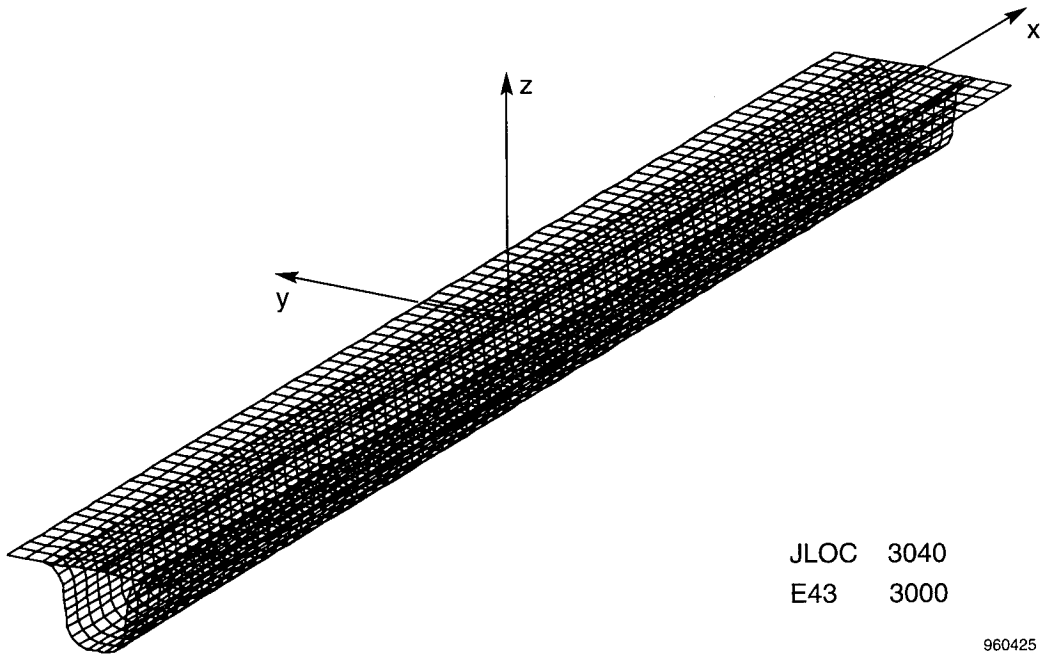

Figure 6. Full-unit strip finite-element model; microbulged face sheet.

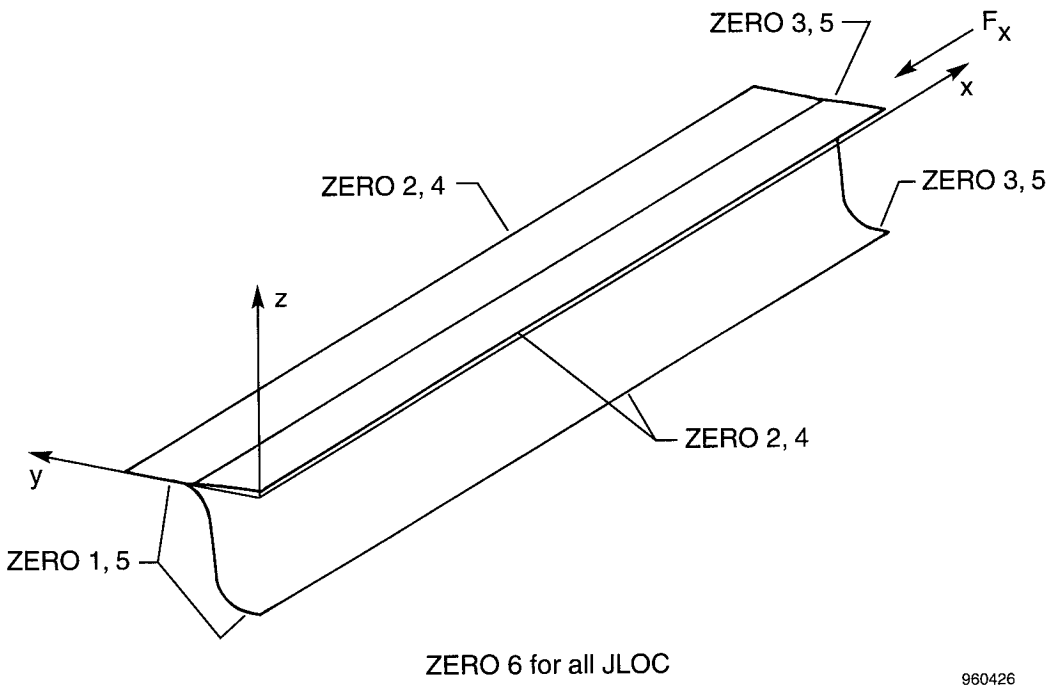

Figure 7. Constraint conditions for axial buckling.

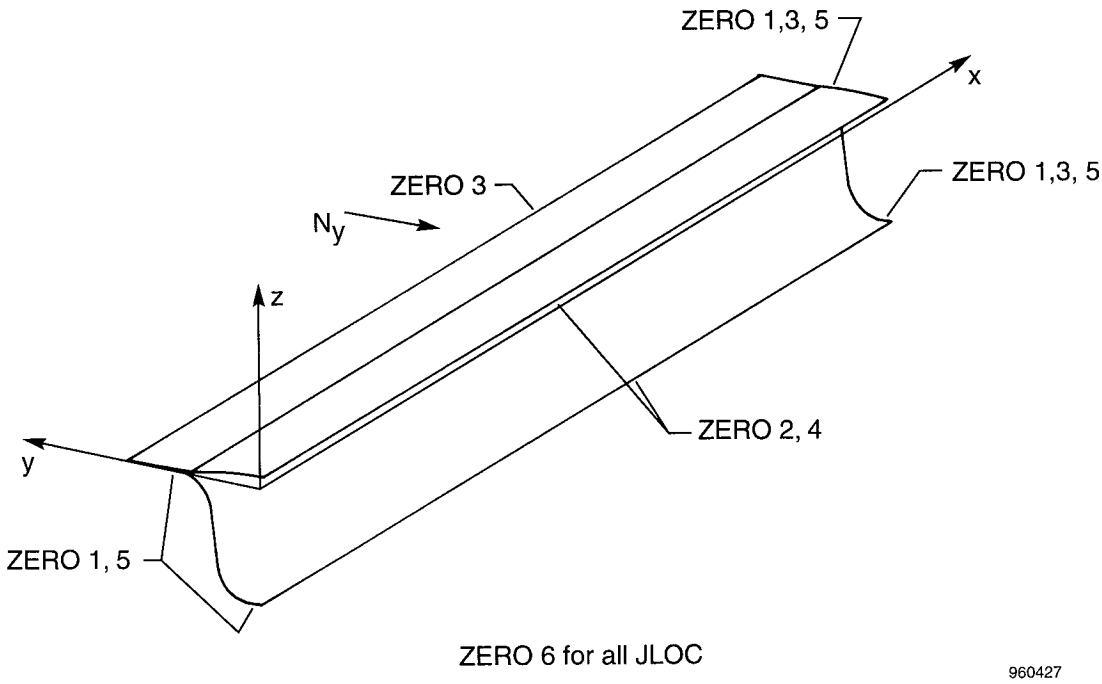

Figure 8. Constraint conditions for lateral buckling.

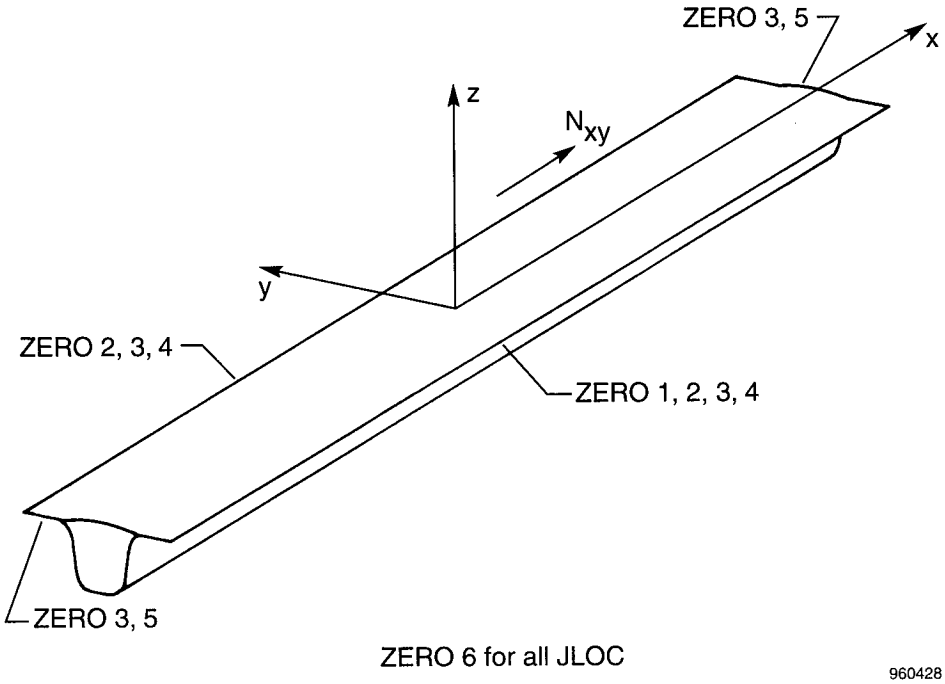

Figure 9. Constraint conditions for shear buckling.

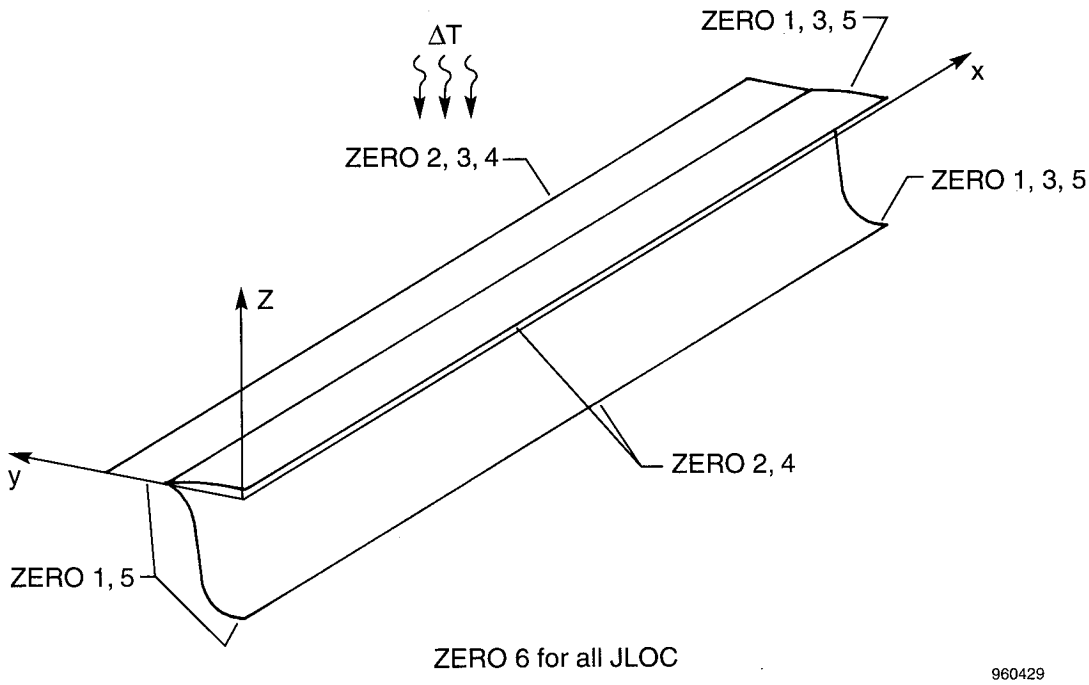

Figure 10. Constraint conditions for thermal buckling.

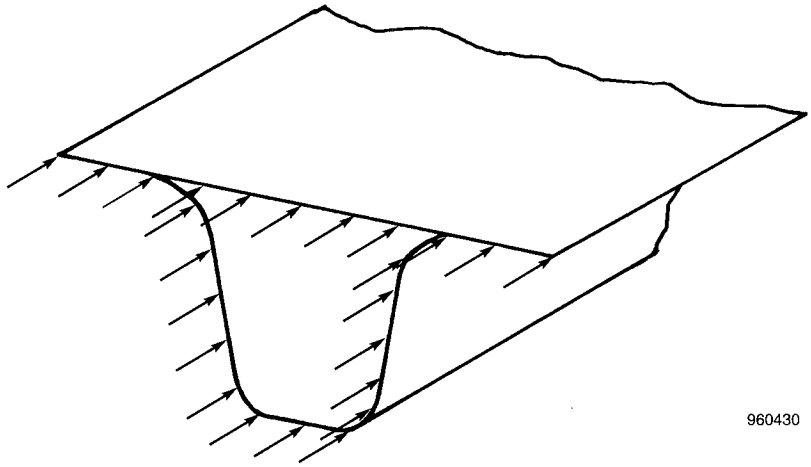

Figure 11. Distributions of applied compressive forces.

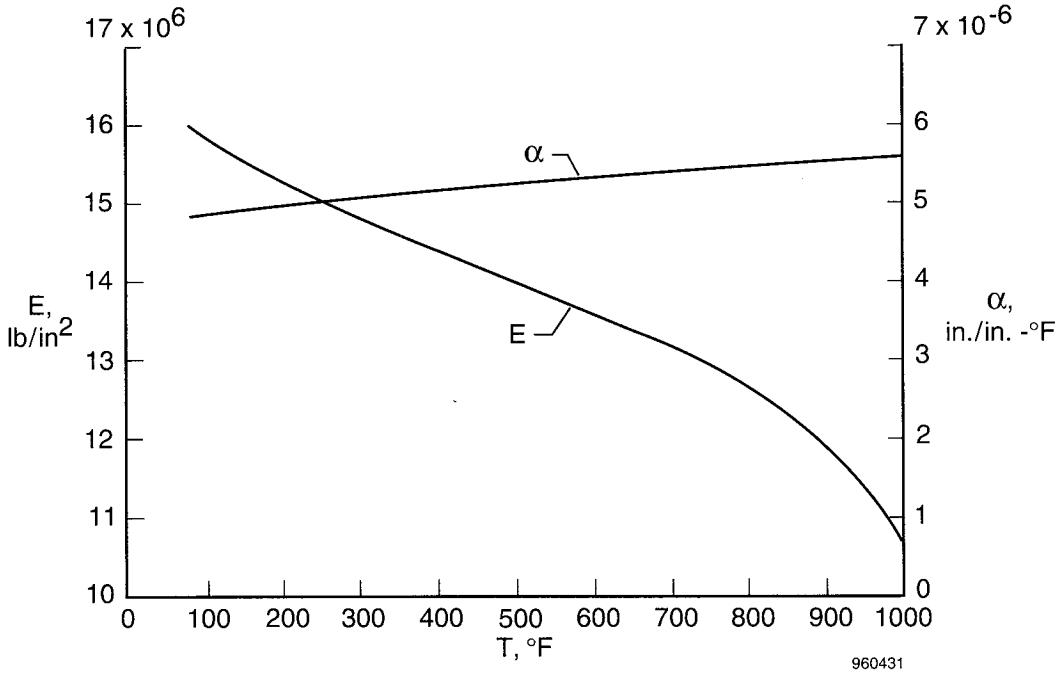

Figure 12. Temperature-dependent material properties; Ti-6A1-4V titanium alloy.

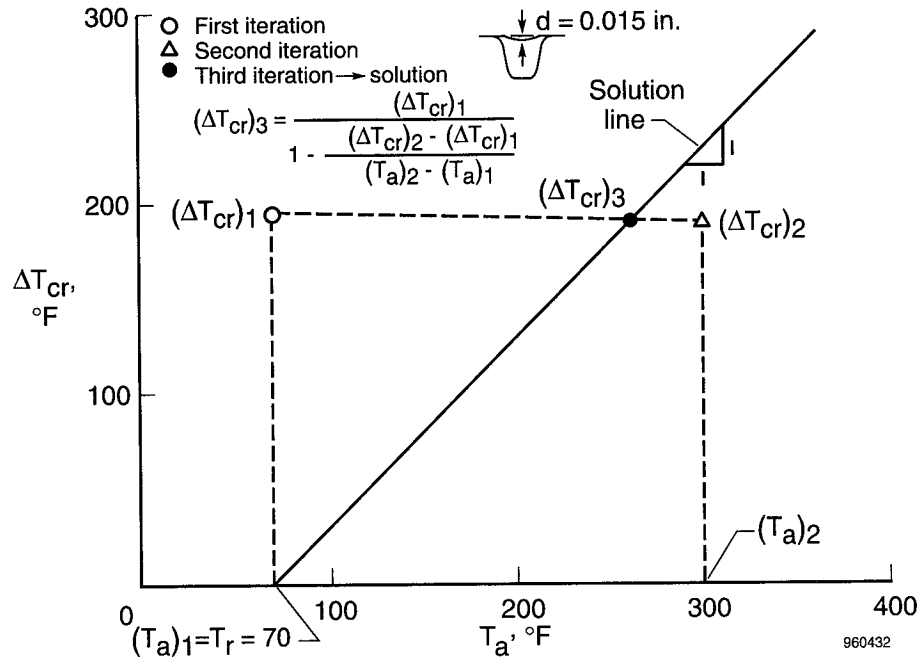

Figure 13. Iterations of buckling temperatures; monolithic hat-stiffened panel; microdented face sheet.

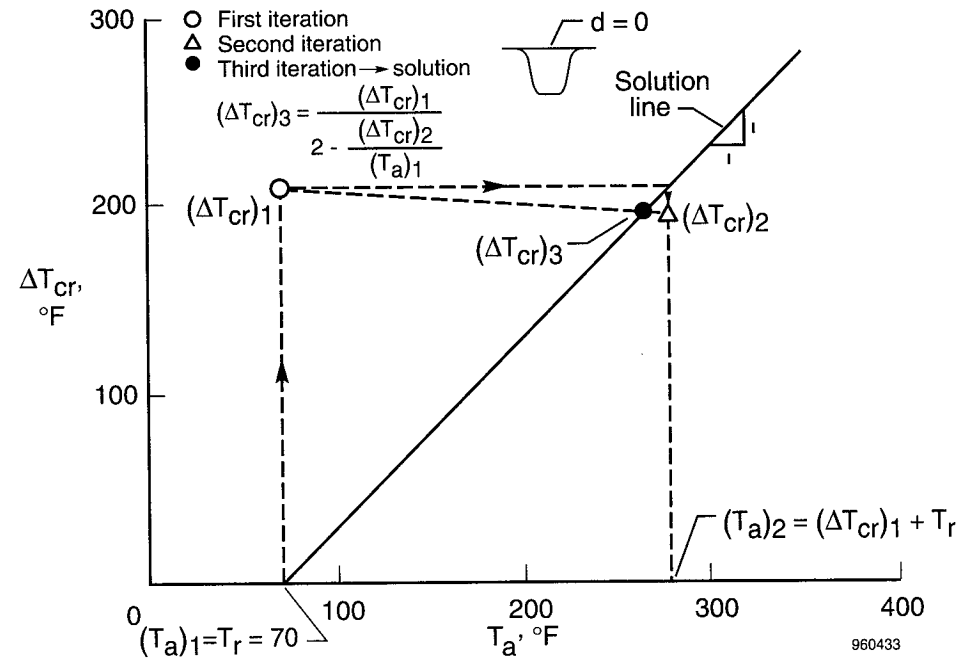

Figure 14. Iterations of buckling temperatures; metal-matrix composite hat-stiffened panel; [90/0/0/90] flat face sheet, [45/–45/–45/45] hat.

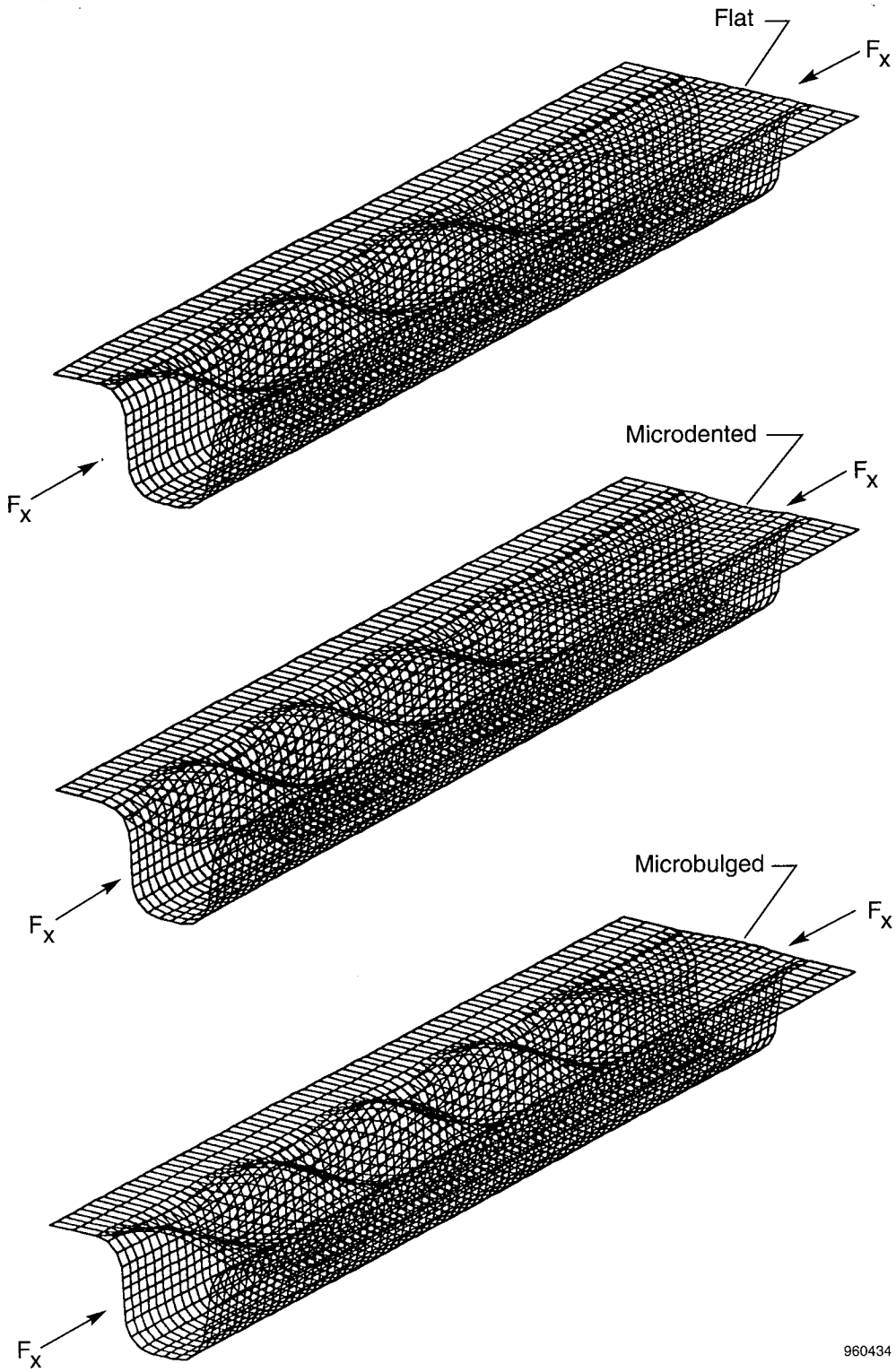

Figure 15. Buckled shapes of three types of hat-stiffened panels under axial compression; monolithic panels.

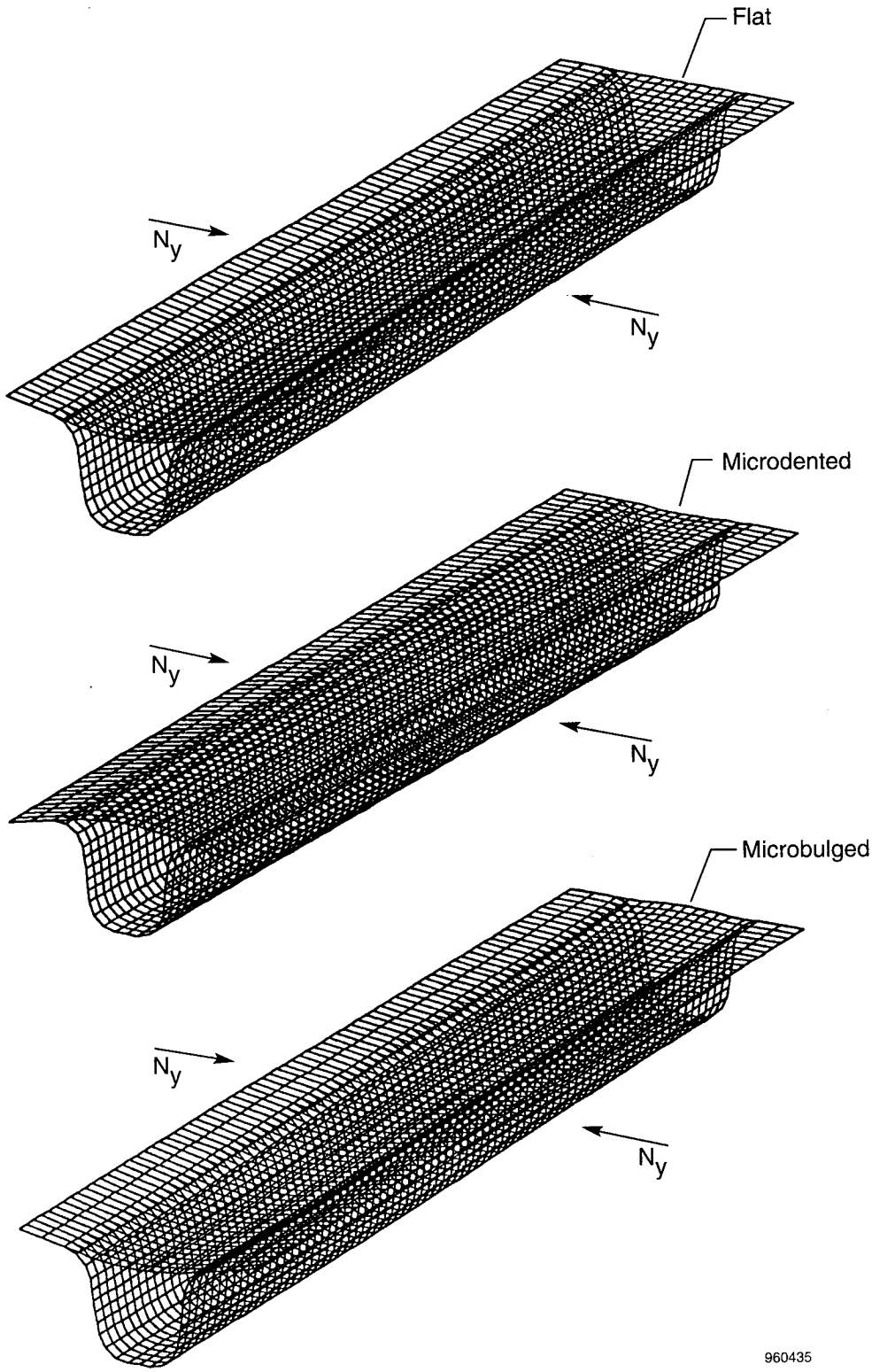

Figure 16. Buckled shapes of three types of hat-stiffened panels under lateral loading; monolithic panels.

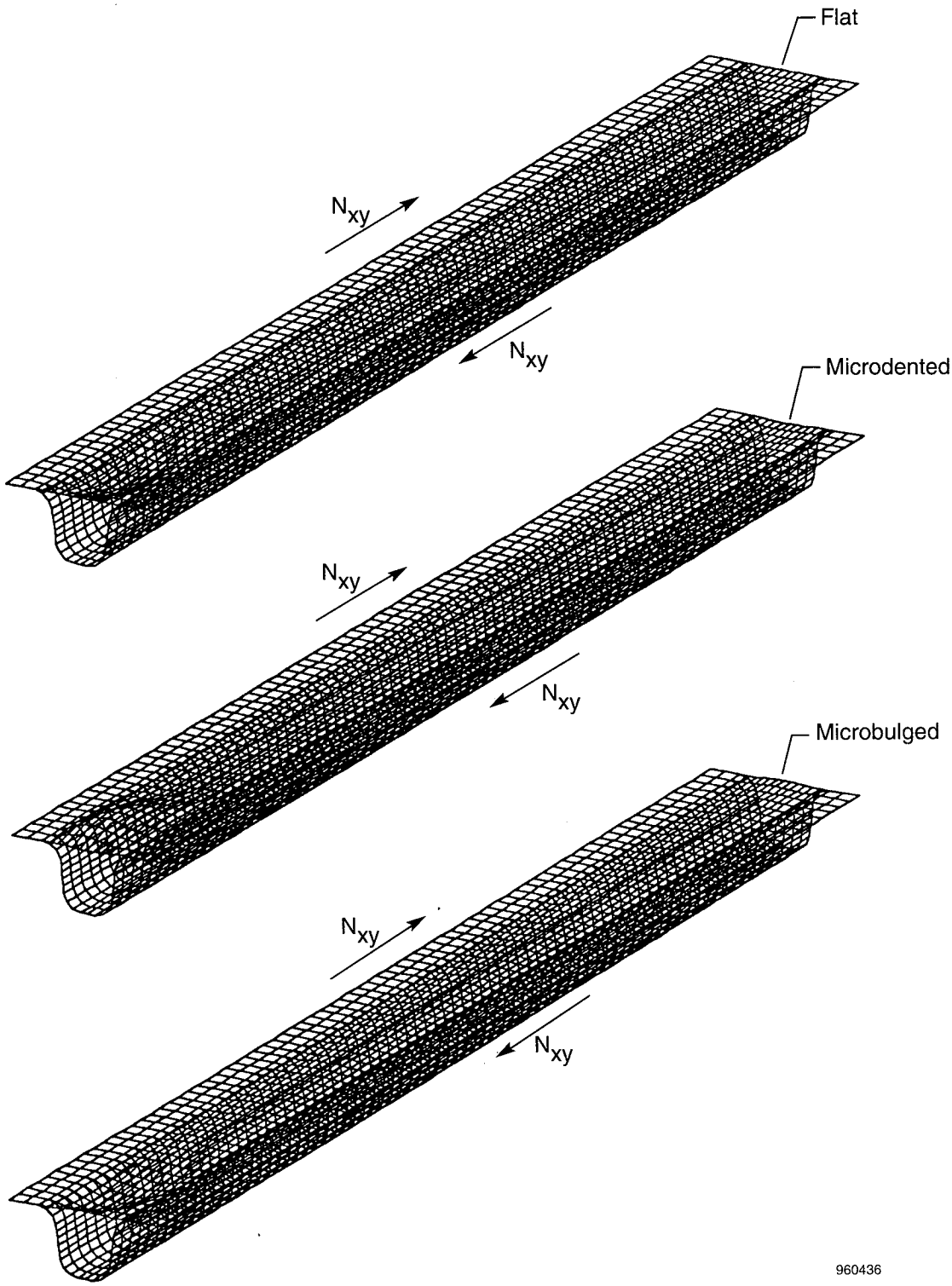

Figure 17. Buckled shapes of three types of hat-stiffened panels under shear loading; monolithic panels.

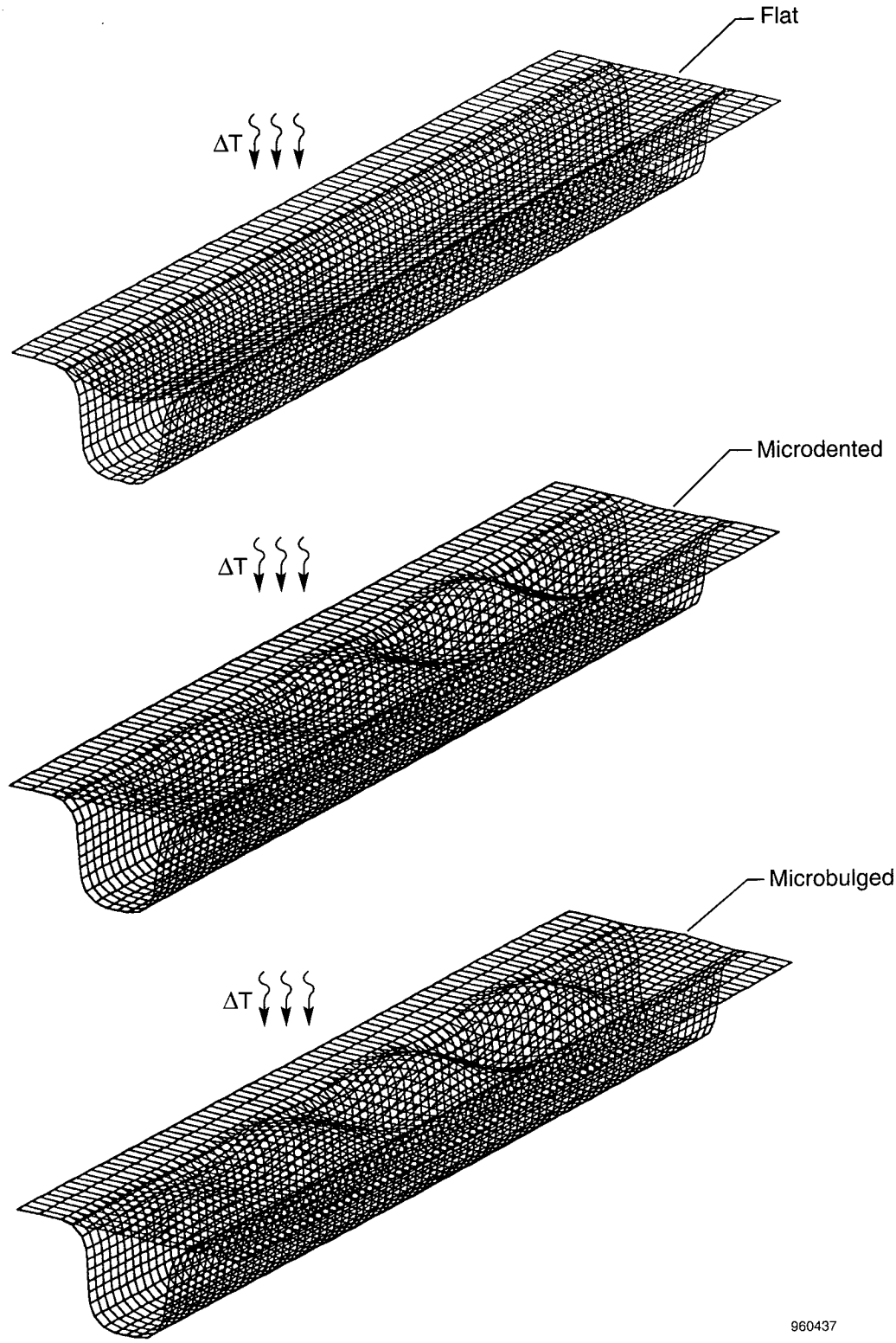

Figure 18. Buckled shapes of three types of hat-stiffened panels under uniform temperature loading; four edges clamped; monolithic panels.

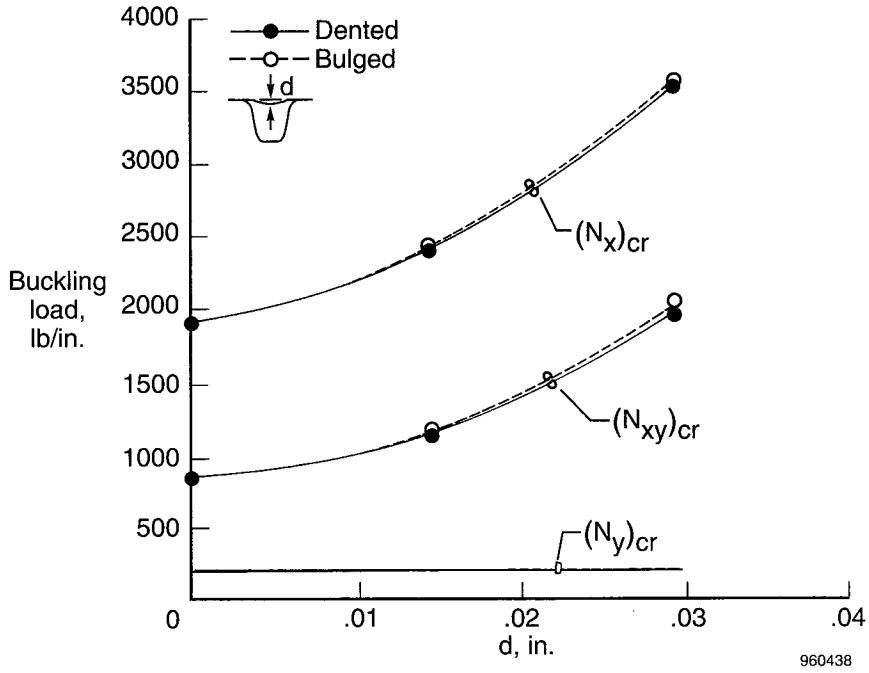

Figure 19. Buckling loads as functions of dent or bulge; monolithic hat-stiffened panels.

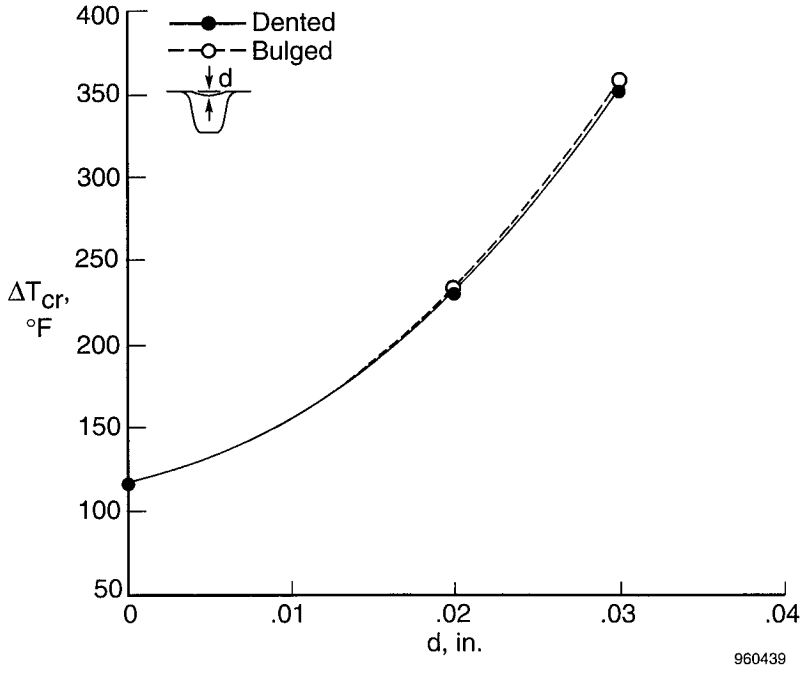

Figure 20. Increase of buckling temperatures with increase of dent or bulge; monolithic hat-stiffened panels.

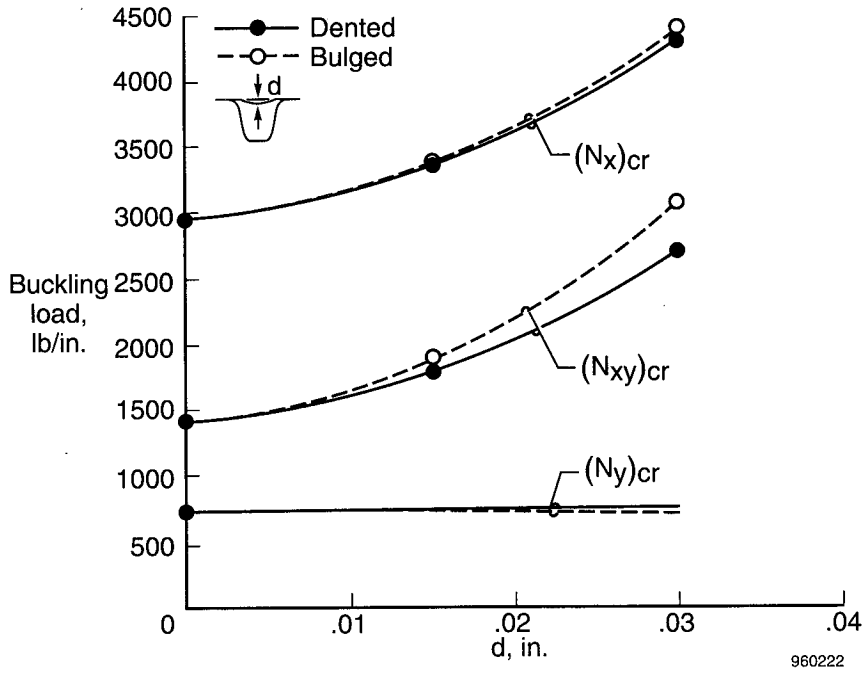

Figure 21. Buckling loads as functions of dent or bulge; metal-matrix composite hat-stiffened panels; [90/0/0/90] face sheet, [45/–45/–45/45] hat.

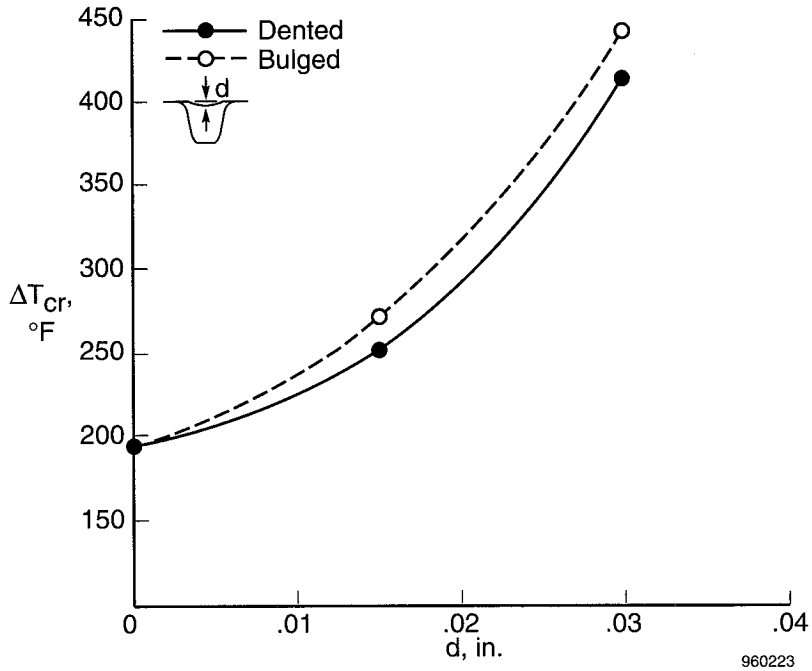

Figure 22. Increase of buckling temperatures with increase of dent or bulge; metal-matrix composite hat-stiffened panel; [90/0/0/90] face sheet; [45/–45/–45/45] hat.

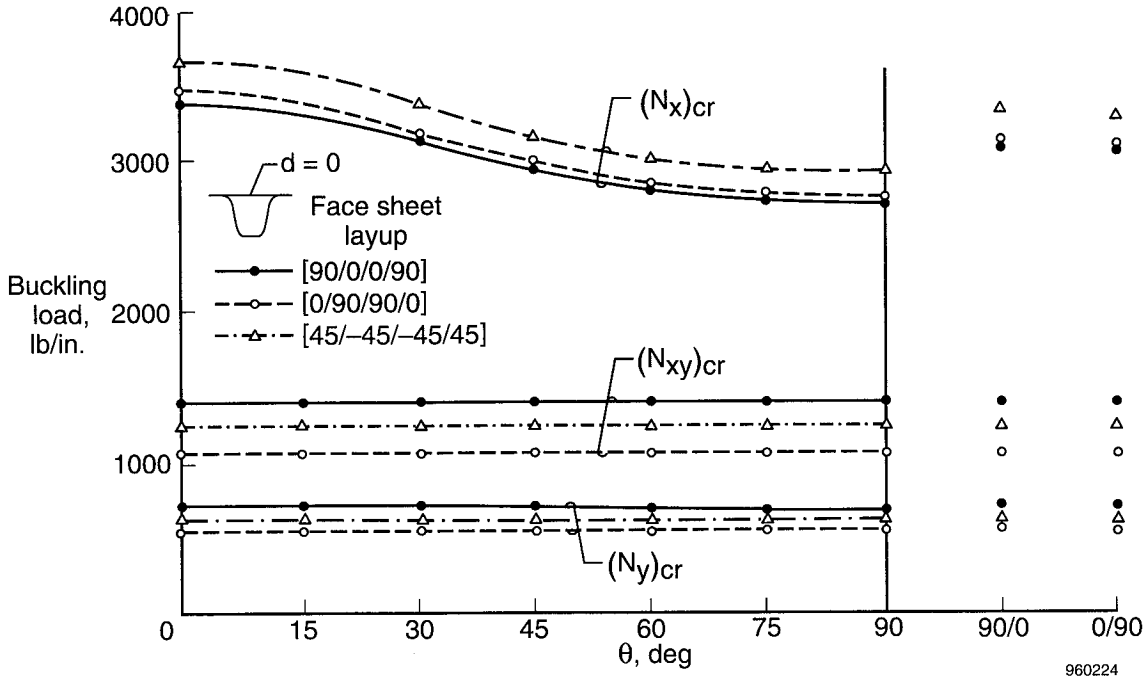

Figure 23. Buckling loads as functions of hat fiber orientation angle; metal-matrix composite hat-stiffened panels with three types of face-sheet layups; flat face sheet ($d = 0$).

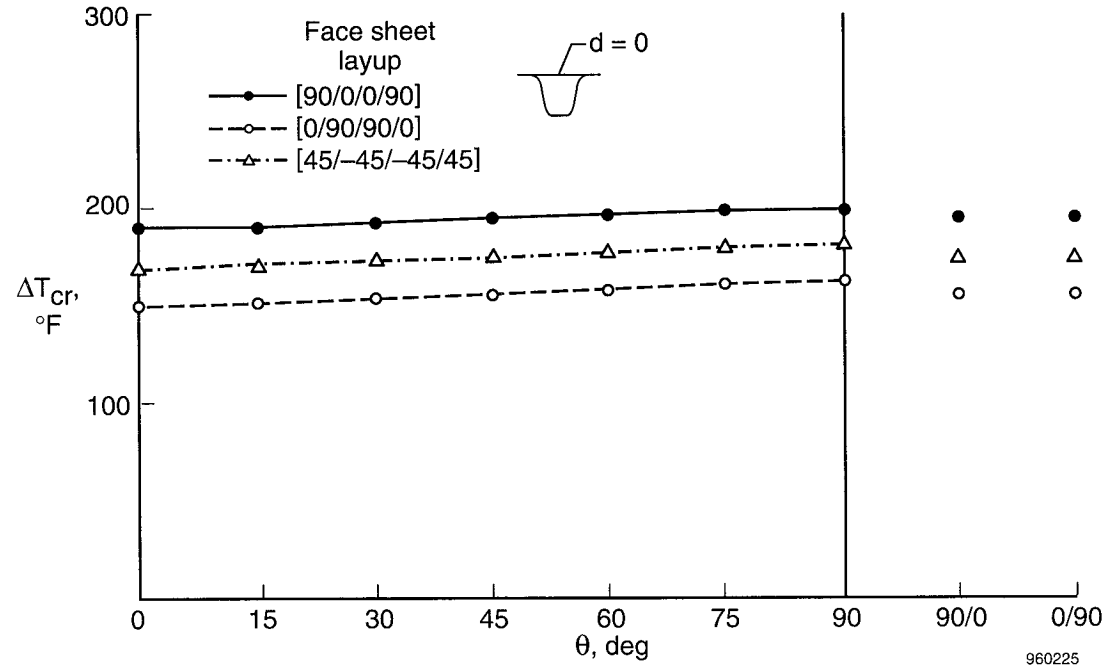

Figure 24. Buckling temperatures as functions of hat fiber orientation; metal-matrix composite hat-stiffened panels; flat face sheet ($d = 0$).